IOP Publishing and International Atomic Energy Agency Nuclear Fusion
Nucl. Fusion **49** (2009) 095025 (10pp) doi:10.1088/0029-5515/49/9/095025

Divertor heat flux mitigation in high-performance H-mode discharges in the National Spherical Torus Experiment

V.A. Soukhanovskii[1,5], R. Maingi[2], D.A. Gates[3], J.E. Menard[3], S.F. Paul[3], R. Raman[4], A.L. Roquemore[3], R.E. Bell[3], C.E. Bush[2], R. Kaita[3], H.W. Kugel[3], B.P. LeBlanc[3], D. Mueller[3] and the NSTX Team

[1] Lawrence Livermore National Laboratory, Livermore, CA, USA
[2] Oak Ridge National Laboratory, Oak Ridge, TN, USA
[3] Princeton Plasma Physics Laboratory, Princeton, NJ, USA
[4] University of Washington, Seattle, WA, USA

E-mail: soukhanovskii2@llnl.gov

Received 31 December 2008, accepted for publication 23 July 2009
Published 4 September 2009
Online at stacks.iop.org/NF/49/095025

Abstract
Experiments conducted in high-performance 1.0 and 1.2 MA 6 MW NBI-heated H-mode discharges with a high magnetic flux expansion radiative divertor in NSTX demonstrate that significant divertor peak heat flux reduction and access to detachment may be facilitated naturally in a highly shaped spherical torus (ST) configuration. Improved plasma performance with high $\beta_t = 15$–25%, a high bootstrap current fraction $f_{BS} = 45$–50%, longer plasma pulses and an H-mode regime with smaller ELMs has been achieved in the strongly shaped lower single null configuration with elongation $\kappa = 2.2$–2.4 and triangularity $\delta = 0.7$–0.8. Divertor peak heat fluxes were reduced from 6–12 to 0.5–2 MW m^{-2} in ELMy H-mode discharges using the inherently high magnetic flux expansion $f_m = 15$–25 and the partial detachment of the outer strike point at several D_2 injection rates. A good core confinement and pedestal characteristics were maintained, while the core carbon concentration and the associated Z_{eff} were reduced. The partially detached divertor regime was characterized by an increase in divertor radiated power, a reduction in ion flux to the plate and a large neutral compression ratio. Spectroscopic measurements indicated the formation of a high-density, low-temperature region adjacent to the outer strike point, where substantial increases in the volume recombination rate and C II, C III emission rates were measured.

PACS numbers: 52.55.Fa, 52.55.Rk

(Some figures in this article are in colour only in the electronic version)

1. Introduction

Candidate techniques for steady-state mitigation of divertor heat and particle loads in future fusion plasma devices must be capable of reducing particle fluxes to the levels of acceptable divertor plate material erosion rates and heat fluxes to $q \simeq 10$ MW m^{-2}, a limit imposed by the present day divertor material and engineering constraints. The techniques must also be compatible with high-performance high-confinement (H-mode) core plasmas and particle control methods. At present, candidate mitigation strategies for ITER and next step fusion devices include both the passive techniques, such as divertor geometry, and active techniques, such as radiative divertors and field ergodization [1–3]. The radiative divertors use deuterium and/or impurities to reduce divertor particle and heat fluxes through volumetric momentum and energy dissipative processes—the ion–neutral elastic and inelastic collisions, recombination and radiative cooling [1]. The effectiveness of radiative divertors depend on many factors [1], the magnetic configuration and magnetic balance among them, as highlighted by recent tokamak studies [4]. Specialized divertor geometry configurations take advantage of the poloidal magnetic flux expansion to reduce particle and heat flux density on divertor targets, as well as the target inclination down to $\simeq 1^\circ$ with respect to the incident field lines, and the extended connection length to radiate additional

[5] Author to whom any correspondence should be addressed.

power [3, 5]. Closely coupled to the development of the mitigation techniques are experimental studies of the scrape-off layer (SOL) transport and turbulence that provide validation of divertor models and novel designs [1, 2].

Substantial experimental work has been carried out on the radiative divertor and divertor geometry effects in tokamaks [1, 2]. In a low aspect ratio spherical torus (ST) magnetic geometry, an inherently large divertor figure of merit P/R [6] (where P is the input power and R is the major radius) and a number of ST SOL and divertor geometry features lead to high divertor heat fluxes [7, 8], raising concerns over divertor operation in the proposed ST-based concepts, e.g., the Component Test Facility (CTF) [9] and the National High-power Advanced Torus eXperiment (NHTX) [10]. Both concepts employ the radiative divertor and/or mantle with high radiated power fractions.

This paper reports on the recent radiative divertor experiments in the National Spherical Torus Experiment (NSTX): a significant peak heat flux reduction simultaneously with good core plasma confinement has been demonstrated in high performance 1.0–1.2 MA, 6 MW NBI-heated H-mode discharges. Access to the radiative divertor regime was previously studied in NSTX in 2–6 MW NBI-heated H-mode discharges in a weakly shaped lower single null (LSN) configuration (a range of elongations $\kappa = 1.8$–2.0 and triangularities $\delta = 0.40$–0.50) using a high D_2 injection rate generally incompatible with H-mode confinement [11, 12]. Experiments conducted in 0.8–1.0 MA, 4–6 MW NBI-heated H-mode discharges in a highly shaped LSN configuration, however, demonstrated reliable access to the partially detached divertor (PDD) regime. The peak heat flux q_{pk} at the outer strike point (SP) was successfully reduced from 4–6 to 0.5–2 MW m^{-2} using divertor deuterium injection with minimal core and pedestal confinement deterioration [13]. In this work, we demonstrate the successful divertor peak heat flux mitigation at the highest divertor heat flux values in the highly shaped configuration, and discuss new insights into NSTX high flux expansion divertor properties enabled by new divertor diagnostic data.

2. Experiment

NSTX is a medium size spherical tokamak with a major radius $R = 0.85$ m, minor radius $a = 0.67$ m and an aspect ratio $A = 1.4$–1.5. Auxiliary plasma heating is achieved by neutral beam injection (NBI) from three sources with 90 kV energy each. The NSTX divertor consists of horizontal and tilted ($\theta = 24°$) toroidally extended copper plates covered with 1.25 cm thick ATJ graphite tiles as shown in figure 1(*a*). The tiles act as plasma-facing components (PFCs). Both NSTX upper and lower divertor plates are up–down symmetric. Both divertors have open geometry enabling much flexibility in plasma shaping.

The NSTX plasma control system [14, 15] was used to obtain a highly shaped LSN configuration with $\kappa \simeq 2.2$–2.4, $\delta \simeq 0.8$ and the δ_{rsep} parameter, the mid-plane distance between the primary and the secondary separatrices, between 8 and 12 mm (figure 1(*b*)). This configuration is referred to henceforth as an LSN configuration, although the secondary (upper) X-point was inside the vacuum vessel and

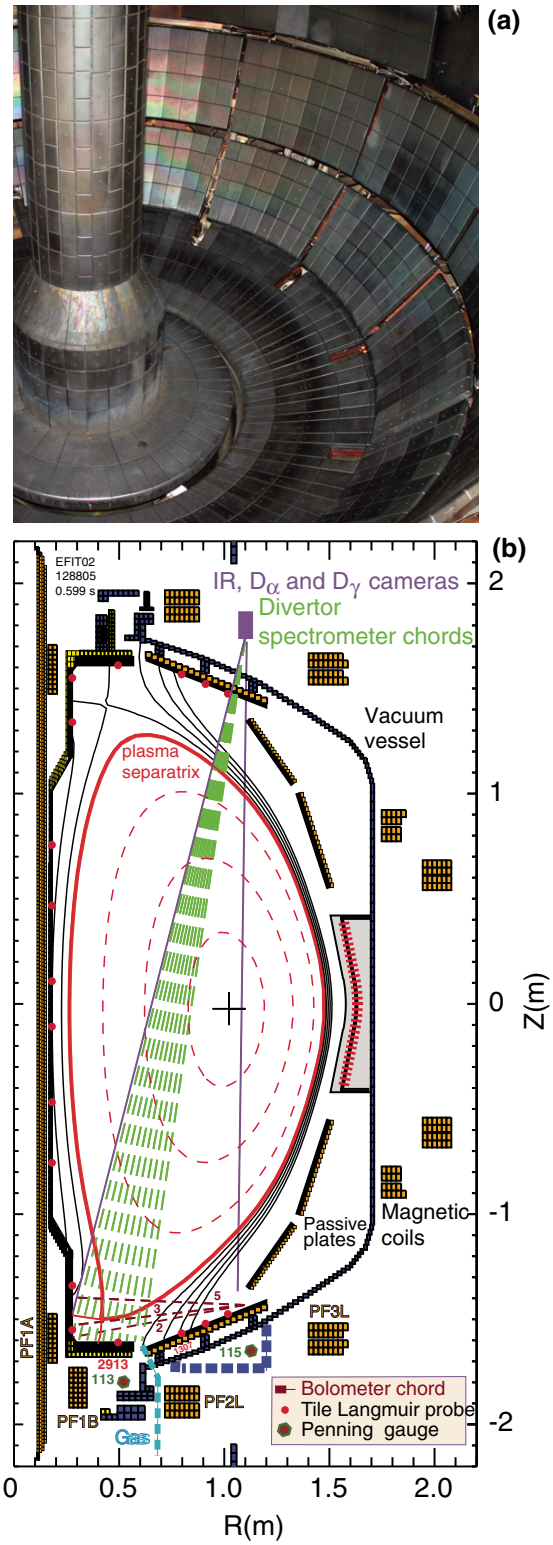

Figure 1. (*a*) Photograph of NSTX divertor, (*b*) plasma equilibrium and layout of divertor diagnostics.

the configuration may also be referred to as a LSN-biased double null configuration. In this configuration, the inner SP was located on the vertical graphite tile target (inner wall), while the outer SP was located on the horizontal graphite target. The ion ∇B drift direction was towards the lower X-point. The toroidal field B_t was 0.45 T. A salient feature

of this highly shaped configuration was a high magnetic flux expansion $f_m = 15$–25, and simultaneously, a high divertor area expansion $A_{exp} = f_m R_{OSP}/R_{MP} = 3.5$–$7.8$. The poloidal magnetic flux expansion is defined here as $f_m = (B_\theta/B_{tot})_{MP}(B_\theta/B_{tot})^{-1}_{OSP}$, where B_θ is the poloidal magnetic field and B_{tot} is the total magnetic field, both evaluated at the mid-plane separatrix (R_{MP}) and at the outer strike point (R_{OSP}). In figure 1(*b*), normalized SOL flux contours separated by 9 mm in the mid-plane are shown. The divertor SOL is defined as a SOL region where both the inner and the outer divertors are fully connected by magnetic flux surfaces. Outside of the divertor SOL, in the far SOL region, magnetic field lines connect the lower divertor and the upper divertor targets.

A comprehensive SOL and divertor diagnostic set has been developed on NSTX (figure 1(*b*)). The diagnostic details can be found in [11–13]. The primary diagnostics for this study were the infrared microbolometer cameras [8, 16], one-dimensional spectrally filtered CCD arrays [17], a 0.5 m commercial ultraviolet–visible (UV–VIS) spectrometer [18], tile Langmuir probes of the flush-mounted design [19, 20], as well as microionization and Penning neutral pressure gauges [21]. Recent facility and diagnostic upgrades were aimed at (1) improved control of divertor gas injection and (2) improved measurements of radiation and neutrals to elucidate on the power and momentum balance in the divertor. These upgrades are briefly described as follows. A new divertor gas injector with a piezoelectric valve enabled D_2 injection into the outer SOL at a constant flow rate up to 200 Torr l s^{-1} (1.4×10^{22} s^{-1}). The flow rate was controlled by pre-filling the injector plenum to a certain calibrated pressure. The gas release was controlled by fully opening the valve which had a characteristic time response of 2–3 ms. To improve the spatial resolution of the previously reported impurity and deuterium line emission measurements [13], a new ten channel interface was developed for the divertor UV–VIS spectrometer [18]. This enabled a ten point profile measurement of impurity and deuterium line emission over most of the lower divertor area. An upgrade to the divertor bolometer system included new detectors and also provided higher spatial resolution of the radiated power measurements in the outer divertor leg. An additional Penning gauge was installed in the outer divertor region, to complement the existing mid-plane and divertor pressure measurements [21]. The neutral pressure measurements were not conductance-limited.

3. High-performance H-mode discharges with radiative divertor

The highly shaped configuration with plasma elongation $\kappa \simeq 2.2$–2.3 and triangularity $\delta \simeq 0.7$–0.8, developed in NSTX in recent years, was used to obtain high-performance plasma regimes, thus demonstrating that the relationship between strong shaping and high performance also held true in the low aspect ratio geometry. Improved plasma performance approaching the performance level of CTF with high $\beta_t = 15$–25%, high $\beta_N \leqslant 5.7$ and a high bootstrap current fraction $f_{BS} = 45$–50% sustained for several current redistribution times has been achieved in highly shaped plasmas in NSTX [14, 22]. This configuration also enabled a routine attainment of an attractive small-ELM H-mode regime [23], providing a basis for a high-performance scenario for future ST-based devices.

Radiative divertor experiments conducted in the highly shaped configuration demonstrated the benefits of increased shaping for divertor heat flux management. The high divertor magnetic flux (and area) expansion led to reduced particle and heat fluxes on the divertor plate, and facilitated access to the outer SP detachment [13]. In this work we demonstrate successful radiative divertor operation in high performance 1.0–1.2 MA H-mode discharges with 6 MW NBI heating. Steady-state measurements of outer divertor heat flux in the NSTX at low κ, δ showed that the peak heat flux q_{pk} increased monotonically with P_{NBI} and I_p, whereas the heat flux width λ_q decreased with I_p [24]. The q_{pk} trend is understood as the corresponding increase in P_{SOL} from the external and ohmic heating powers, and the decrease in connection length $L_\parallel$ ($L_\parallel$ is proportional to the safety factor). To the lowest order, this provided a quantitative explanation for the q_{pk} dependence on P_{SOL} and a qualitative explanation for the I_p trend. Because of $q_\parallel = P_{SOL}/A_\perp = P_{SOL}/(4\pi R(B_p/B_{tot})\lambda_q)$, the discharges with $I_p = 1.0$–1.2 MA and $P_{NBI} = 6$ MW result in the highest SOL parallel heat flux, estimated to be $q_\parallel \simeq 50$–80 MW m^{-2}. The radiative divertor technique employed divertor D_2 injection that increased divertor density, recycling and neutral pressure. The associated increases in radiated power and ion momentum loss through charge exchange, elastic collisions and eventually recombination, led to a reduction in heat and particle fluxes in the outer SP region. Many characteristics of the NSTX PDD regime were similar to the PDD regimes induced by extrinsic deuterium injection (e.g. [25]) and/or occurring naturally at high plasma density (e.g. [26, 27]) in large aspect ratio tokamaks. In this section we discuss core, SOL and divertor measurements that contributed to a consistent picture of the partially detached OSP regime in NSTX. The inner divertor strike point typically detached at early time (low $\bar{n}_e$) and remained detached throughout the discharge duration, as a result of the low SOL power flow, proximity of the inner wall and higher inner leg n_e due to inner wall gas fuelling. The ISP was detached in nearly all NBI-heated H-mode discharges in NSTX [13, 28].

An important objective of this experiment was to demonstrate the radiative divertor operation in NSTX with minimal core and pedestal plasma performance degradation. Core conditions are illustrated for the reference 1.0 MA and 1.2 MA 6 MW H-mode discharges and for the discharges with divertor D_2 injection in figure 2. A transition to the PDD regime occurred within 30–70 ms from the start of the D_2 injection in both cases. Core plasma stored energy degraded by 5–15% during the PDD phase. Core plasma β_t was maintained in the range 16–22 throughout the I_p flat-top. The energy confinement time in the H-mode phase was $\tau_E \simeq 40$–60 ms, in the range 1.6–1.8 of the ITER89P confinement scaling factor. Plasma T_e and n_e profiles measured by the Thomson scattering system showed that in general, pedestal T_e decreased and n_e increased by about 5–15%. As in previous radiative divertor experiments in NSTX [11, 13], divertor gas injection led to a large core carbon concentration and radiated power reduction. The main impurity identified by vacuum ultraviolet and ultraviolet spectroscopy was carbon. Plasma Z_{eff} was in the range 1.5–2.5. Both P_{rad} and Z_{eff} decreased

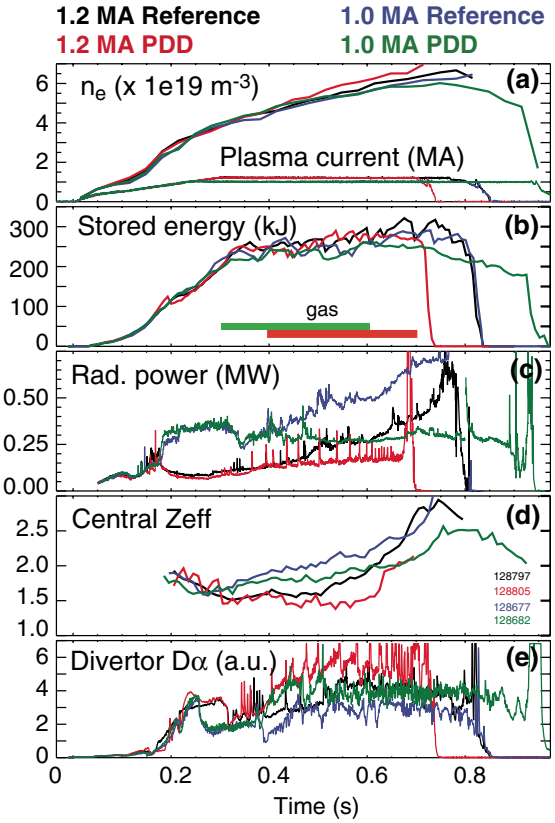

Figure 2. Time traces of the 1.0 and 1.2 MA 6 MW discharges with and without divertor gas injection: (*a*) $\bar{n}_e$, I_p, (*b*) Stored energy, gas injection (*c*) Core P_{rad}, (*d*) Central Z_{eff}, (*e*) Divertor D_α.

substantially, by 20–30%, in the PDD phase. This decrease could be attributed in part to the large type I ELMs that appeared as a result of gas puffing in the 1.2 MA discharges and expelled impurities from the core. However, in the 1.0 MA discharges the gas puffing did not affect the reference, small-ELM regime, yet a similar reduction in P_{rad} and Z_{eff} took place. The core carbon concentration reduction could be due to magnetohydrodynamic (MHD) activity, a reduction in the carbon edge source and due to changes in radial impurity transport. Two MHD modes, with toroidal numbers $n = 2$ and $n = 3$, were identified in these discharges, and the gas injection did not seem to have any impact on their frequency and duration. This result suggests further studies of the carbon source and core transport effects in the PDD regime in NSTX. Large aspect ratio tokamak experiments demonstrated that gas puffing and OSP detachment can have measurable effects on the divertor carbon source by reducing carbon chemical and physical sputtering rates [29], on the edge radial electric field, and on SOL ion and impurity flow pattern through the parallel momentum balance (viscosity), propagating the latter effect to the edge and core impurity transport [30, 31].

A partial detachment of the outer SP has been obtained at several gas puffing rates Γ_g. Summarized in figure 3(*a*) are the peak heat flux q_{pk} measurements at progressive times for a number of gas puffing rates for the 1.0 and 1.2 MA discharges. For comparison, measurements of highest q_{pk} in reference discharges (without gas injection) are also shown. In general, higher gas puffing rates were necessary to reduce q_{pk} in 1.2 MA discharges, where $q_\parallel$ was higher, in comparison with 1.0 MA discharges, as $q_\parallel$ and λ_q depend on I_p. As evident from the figure, higher Γ_g led to a faster q_{pk} reduction. However, after about 250–270 ms, peak heat fluxes reached steady-state low levels of about 1 MW m^{-2} in the 1.0 MA discharges, and about 1.5–2.0 MW m^{-2} in the 1.2 MA discharges. The optimization of the gas injection entailed using the rate and gas pulse duration that reduced q_{pk} on a time scale of 100–200 ms yet caused a minimal reduction in confinement and did not lead to an X-point MARFE formation over 0.5–0.7 s. For the 1.0 MA discharges, this rate was found to be $\Gamma_g \leqslant 100$ Torr l s^{-1}, while for the 1.2 MA discharges it was in the range 110–160 Torr l s^{-1}, as follows from the stored energy trend shown in figure 3(*b*) and the plasma current I_p end of flat-top times (figure 3(*c*)). Qualitatively, higher level gas puffing led to a more resistive plasma (higher $\bar{n}_e$, lower T_e), thus a higher inductive flux consumption (higher normalized internal inductance l_i, not shown); an earlier formation of a highly radiative X-point MARFE, thought to be detrimental to high confinement. This experience was similar to large tokamak experiments with open geometry divertors operated without active pumping [1].

Outer divertor heat flux profiles, measured between large and medium ELMs and averaged over small ELMs, showed a substantial reduction in divertor heat load during the PDD phase. Shown in figure 4 are divertor heat flux profiles for the 1.0 and 1.2 MA discharges discussed above. In both cases, a 40–70% decrease in heat flux was measured in a ~10 cm radial zone adjacent to the outer SP. The extent of the detachment zone was within 50–80% of the full divertor SOL width. Heat flux profiles did not change outside of the detachment zone, remaining at the level 0.5–1.0 MW m^{-2}.

Partial detachment characteristics pertaining to the outer divertor power and momentum balances will now be discussed using the 1.2 MA discharge data. Time traces of the SOL and divertor power balance components for the 1.2 MA case are shown in figure 5. They confirmed that divertor radiated power accounted for much of the divertor power loss. From the total SOL power of $P_{SOL} = 4.5$–5 MW, the outer divertor target received about 2–3 MW in the reference discharge, and 1–2 MW in the PDD discharge, as shown in figure 5(*b*). From the 5–15% difference in Q_{div}/P_{SOL} between the reference and PDD discharges, the divertor radiated power could be inferred $P_{rad}^{div} \leqslant 0.2$–0.7 MW. Intrinsic carbon impurity and deuterium were identified as the main radiating species responsible for divertor power loss, as discussed later in this section. The power flow into the upper divertor was negligible, as would be expected in the LSN-biased configuration. This was confirmed by IR camera measurements. It was not possible to measure the total lower divertor radiated power with the present bolometer system (figure 1) as the uncertainties in radiation distribution viewed by only two nearly horizontal chords could lead to P_{rad}^{div} uncertainties of ±50% or even higher [32]. Divertor bolometer signals representative of the outer divertor leg (chord 3, below the X-point) and edge (chord 5, above the X-point) did show an increase in brightness. However, the chord 2 brightness, representative of the region above the outer SP, was lower in the PDD case (figures 5(*c*) and (*d*)). A direct comparison between the plasma brightness traces in the reference and the PDD discharges was complicated by the fact that the two

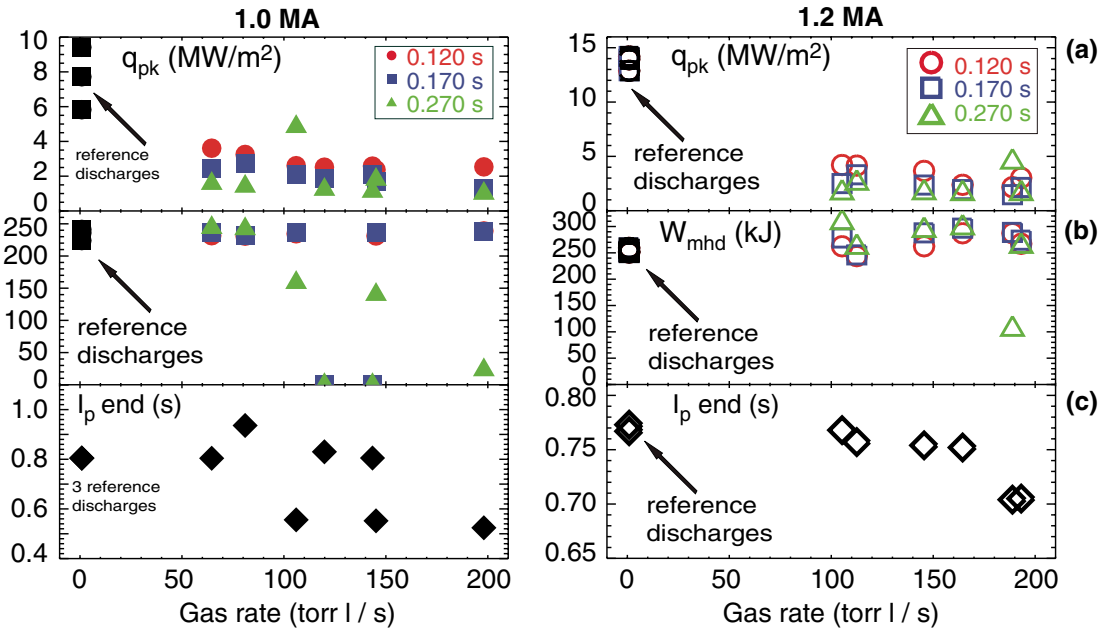

Figure 3. Divertor q_{pk} (*a*), plasma stored energy W_{MHD} (*b*) and end time of plasma current I_p flat-top (*c*), for 1.0 MA (left column) and 1.2 MA (right column) PDD discharges as a function of divertor gas injection rate at 120, 170 and 270 ms after the start of gas injection. Note that 1 Torr l s^{-1} = 7 × 10^{19} s^{-1}.

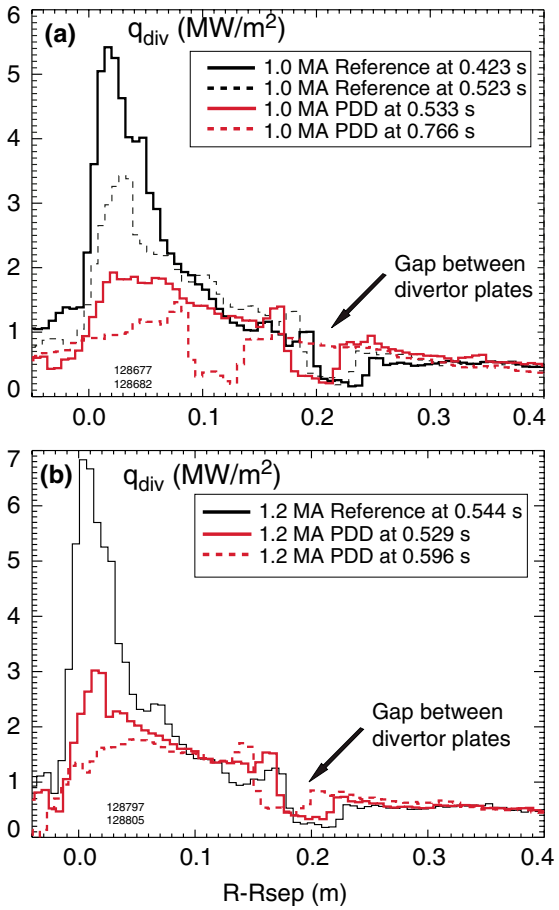

Figure 4. Divertor heat flux profiles in the reference and PDD discharges: (*a*) 1.0 MA and (*b*) 1.2 MA.

divertor bolometer chords measured radiation above the outer SP and below the X-point, thus potentially missing the regions where much radiation occured in the PDD discharge. Another issue was that the radiation front, a region of the maximum carbon radiation efficiency with $T_e \simeq 10$ eV, was likely to move up along the divertor leg after the PDD onset, as the parallel temperature gradient steepened and T_e in the outer SP region decreased, as observed in large aspect ratio tokamaks (e.g. [33]). The transient increase in divertor plasma radiation measured by the bolometer at the PDD onset (figure 5(*d*)) was suggestive of the formation and motion of the radiation front (while not associated with a large ELM or plasma movement).

During the detachment, parallel plasma pressure loss results in the reduction in the particle flux to the divertor plate. Experimental evidence for this is the Langmuir probe ion saturation current density 'roll-over', or in some cases, constant value, in the detachment zone, while the divertor D_α intensity continues to increase due to recombination [1, 34]. Shown in figures 6(*a*) and (*b*) are the outer divertor ion flux density Γ_i time traces of two divertor Langmuir probes. The parallel ion flux density was obtained from $j^+_{sat} = I_{sat} A^{-1}_{probe}$ measurements: $\Gamma_i = j^+_{sat}(e \sin\gamma)^{-1}$, where e is the electron charge, γ is the angle between the total magnetic field and the probe tip surface and A_{probe} is the probe tip collection area. Probe locations are shown in figure 1. Probe 2913 was located with a distance ranging from 9 cm to 11 cm from the OSP, marginally inside the PDD zone. The Γ_i measured by this probe remained low during the gas injection and OSP detachment, and eventually reduced, while D_α intensity substantially increased (figure 6(*c*)). Probe 1307 was located in the far SOL region connected by magnetic field lines to the upper divertor. The increase in the Γ_i measured by the probe, as well as the D_α intensity at the probe location, were well correlated with the divertor gas injection. Shown in

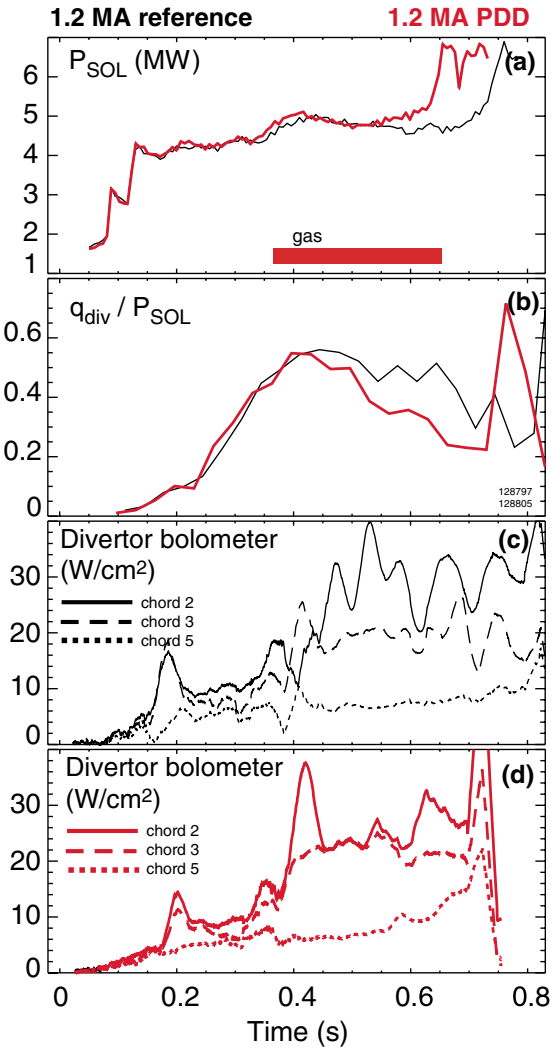

Figure 5. Time traces of the 1.2 MA reference and PDD discharges (*a*) P_{SOL}, (*b*) $Q_{\mathrm{div}}/P_{\mathrm{SOL}}$, Divertor and edge bolometer signals in the reference (*c*) and PDD (*d*) discharges.

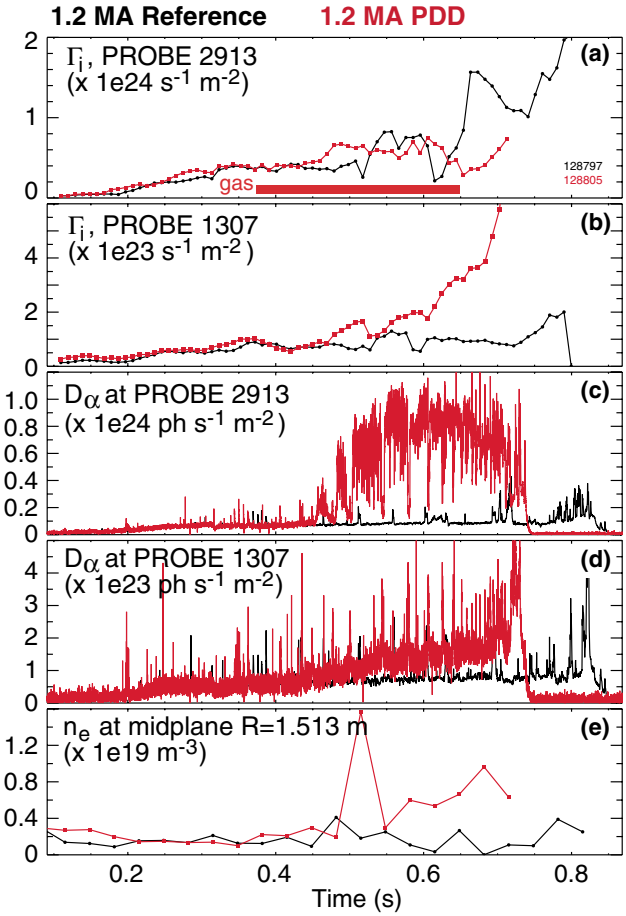

Figure 6. Time traces of (*a*) Γ_{i} measured by Langmuir probe 2913, located at $R = 0.495$ m; (*b*) Γ_{i} measured by Langmuir probe 1307, located at $R = 0.797$ m; (*c*) D_α brightness at the divertor $R = 0.495$ m location; (*d*) D_α brightness at the divertor $R = 0.797$ m location in the 1.2 MA reference and PDD discharges; (*e*) n_{e} measured by the Thomson scattering system at the $R_{\mathrm{mid\text{-}plane}} = 1.513$ m location connected with probe 1307.

figure 6(*e*) is the n_{e} time history measured by the Thomson scattering system in the mid-plane at $R = 1.513$ m, a radial region connected by field lines to the Langmuir probe 1307. The plasma control system held the outer separatrix position nearly constant between 0.2 and 0.7 s. The particle flux measured by probe 1307 was found to be a function of the upstream density: $\Gamma_{\mathrm{i}} \sim n_{\mathrm{e}}^{\alpha}$, with $\alpha = 1.5$–2.2, suggesting that the far SOL was in the high-recycling regime during the D_2 injection. The functional dependence $\Gamma_{\mathrm{i}} \sim n_{\mathrm{e}}^2$ and electron collisionality $\nu_{\mathrm{e}}^* \geqslant 15$ are expected in the high-recycling regime based on two-point heat transport model arguments [34]. The electron collisionality in the far SOL during the D_2 injection was estimated to be $\nu_{\mathrm{e}}^* = l_{\mathrm{c}}/\lambda_{\mathrm{e}} \sim 20$–$30$, where l_{c} was the connection length, λ_{e} was the electron mean free path, for $l_{\mathrm{c}} \sim 3$ m from the equilibrium reconstruction, and $T_{\mathrm{e}} = 5$–10 eV, $n_{\mathrm{e}} = (0.2$–$0.8) \times 10^{-19}$ m^{-3} from the Thomson scattering measurements.

The difference between the detached near SOL and high-recycling far SOL region conditions was also apparent in the fast D_α measurements in the ELMy phase (figures 6 (*c*) and (*d*)). The type I ELM heat pulse perturbation caused D_α spikes in the high-recycling region, corresponding to a D_α emissivity increase in response to a transient increase in T_{e} and n_{e}. In the detached region, where the D_α intensity included a large component due to electron–ion recombination, the ELM heat and particle pulse caused a transient re-attachment of plasma, and a transient reduction in recombination rate, thus a 'dip' in the D_α trace. This conjecture is consistent with comprehensive measurements of the SOL response to type I ELMs in DIII-D [35, 36].

Parallel plasma pressure loss in the SOL during detachment is caused by ion momentum loss due to ion–neutral collisions and charge exchange between ions and neutrals. A high neutral density in the divertor must be maintained for these reactions to occur at a substantial rate. It is also desirable to maintain a fairly low neutral pressure in the main chamber, since neutrals can affect the edge electric field and plasma rotation through the toroidal angular momentum flux modification due to charge exchange and thus cause an H–L transition. One way to address this situation is to operate with a geometrically closed divertor which reduces neutral flux from the divertor to the main chamber (e.g. [1, 37]). As previously shown in NSTX, a high magnetic flux expansion

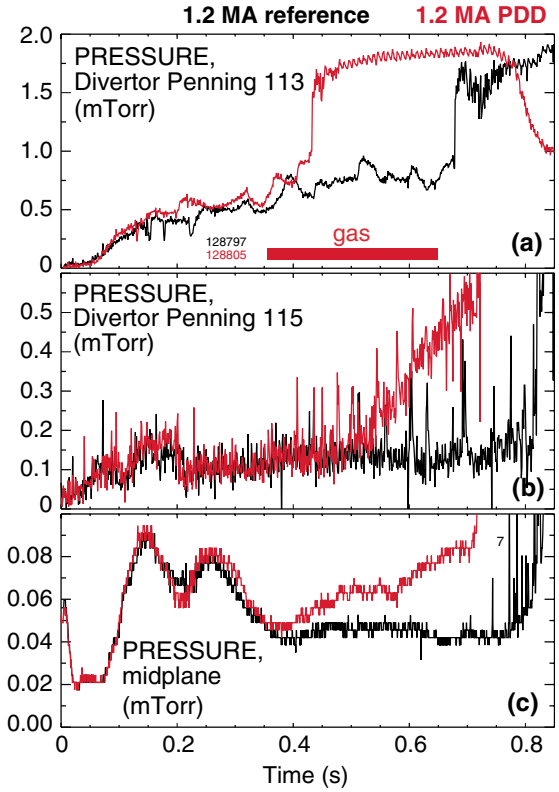

Figure 7. Time traces of neutral pressure in the 1.2 MA reference and PDD discharges: (*a*) neutral pressure in outer divertor region, Penning gauge 113, (*b*) neutral pressure in outer divertor region, Penning gauge 115, (*c*) mid-plane neutral pressure.

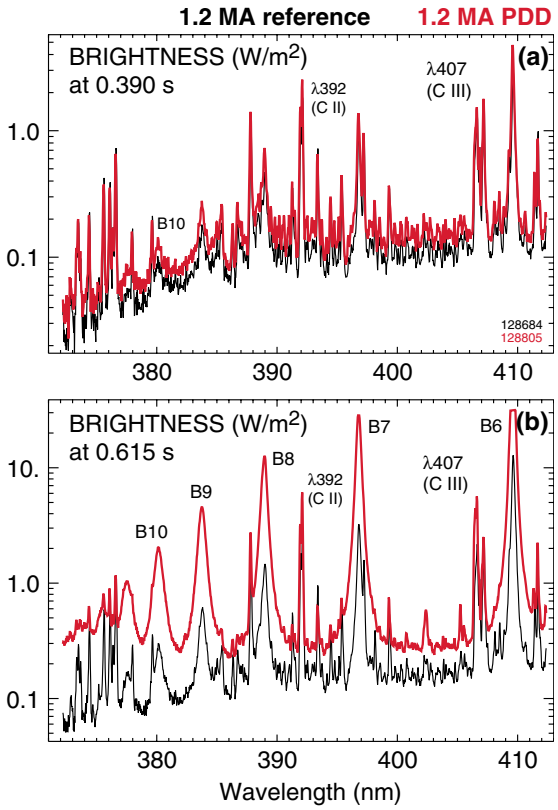

Figure 8. Divertor ultraviolet spectra corresponding to the $R = 0.450$ m in the 1.2 MA reference and PDD discharges at times before (*a*) and after (*b*) divertor gas injection (no gas injection in the reference discharge).

divertor even in an open geometry can provide a high neutral compression ratio due to its high plasma 'plugging' efficiency [13]. This is demonstrated by time traces of neutral pressure in figure 7. A high neutral pressure, $p_n = 0.5$–1.5 mTorr, was maintained in the divertor during the PDD phase, while mid-plane neutral pressure remained low. A two-point divertor Penning gauge measurements indicated a radial gradient in the divertor pressure, confirming that the high neutral pressure (density) zone was localized in the OSP region. The Penning gauges 113 and 115 were not directly affected by gas puffing, as they were toroidally separated from the divertor gas injector by 90° and 30°, respectively.

New insights into divertor detachment dynamics in NSTX were provided by the impurity and deuterium emission profiles measured by multichannel ultraviolet spectroscopy (figure 1). Shown in figure 8 are the OSP region ultraviolet spectra in the reference and the PDD discharges at times before and after the detachment onset. Molecular CD and BD bands seen in all spectra suggest further spectroscopic studies of the role of molecules in the high expansion divertor performance. The Paschen continuum slope, Stark broadening and intensity of deuterium Balmer series lines $n = 2 - m$, where $m = 6$–11 are characteristic of the recombination rate and average divertor T_e and n_e [38–40]. The dynamics of divertor recombination and C II, C III emission were obtained from the spectra. Shown in figure 9 are the brightness contours of the $\lambda = 380$ nm deuterium B10 line, representative of the divertor recombination distribution, the $\lambda = 392$ nm C II line and the $\lambda = 407$ nm C III line, representative of the C II and C III emission distribution in the divertor, respectively. Also shown are time histories of the OSP major radius and a projection of the X-point major radius on the divertor surface along the spectrometer viewing chords (figure 1). In the reference discharge, the recombination took place in the inner divertor and in the 'gas box' gap between the divertor plates around $R = 0.60$ m in the outer divertor region. A large increase in the recombination rate in the region adjacent to OSP and the X-point were apparent in the PDD discharges during divertor D_2 injection. In the same region, based on the developed Stark broadening and line intensity analysis [13, 18], the average plasma conditions were estimated to be $n_e \leqslant (3$–$5) \times 10^{20}$ m^{-3}, and low $T_e \leqslant 1.0$–1.5 eV. The spatial extent of this high-density, low-temperature region was well correlated with other diagnostic time traces (e.g. those shown in figures 6 and 7). The Balmer B10 line emission appeared to peak in the X-point region, suggesting that an X-point MARFE could have formed later in the PDD phase. Both the C II and C III line emission rates also significantly increased after the PDD onset as a result of increasing n_e in the outer divertor region. In the reference discharges, the carbon emission was concentrated in the high-density inner divertor leg. In the PDD discharges, C II profiles appeared to be nearly flat, while the C III profiles were peaked in the PDD zone. Towards the end of the PDD discharge, the carbon emission peaked around the X-point and in the divertor plate gap, both regions of high electron density. The deuterium recombination and carbon emission dynamics were consistent with the two-dimensional picture of the tokamak divertor detachment [41, 33].

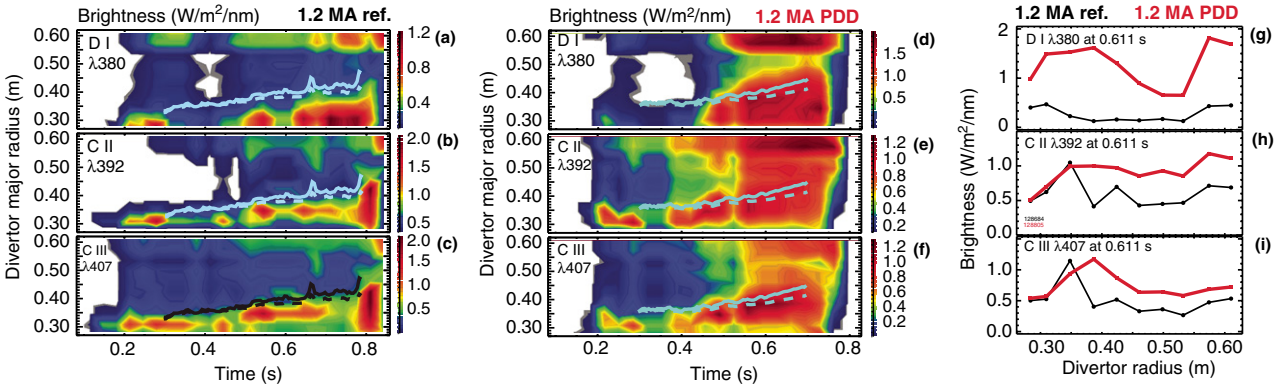

Figure 9. Time histories of divertor line brightnesses and divertor emission profiles. In the 1.2 MA reference discharge: (*a*) deuterium λ380 nm B10 line, (*b*) C II λ = 392 nm line, (*c*) C III λ = 407 nm line; In the 1.2 MA PDD discharge: (*d*) deuterium λ380 nm B10 line, (*e*) C II λ = 392 nm line, (*f*) C III λ = 407 nm line. Panels (*g*), (*h*), (*i*)—Brightness profiles of B10, C II and C III emission in the reference and PDD discharges at 0.611 s. Solid lines show time histories of the OSP major radius. Dashed lines show a projection of the X-point major radius on the divertor along the spectrometer viewing chords.

Table 1. Typical SOL and divertor geometric factors of the NSTX high κ, δ configuration and a tokamak.

Quantity	NSTX	Tokamak
Aspect ratio	1.4–1.5	2.7
In-out plasma boundary area ratio	1 : 3	2 : 3
Mid-plane to target connection length l_c (m)	8–10	30–80
X-point to target parallel length l_x (m)	5–7	10–20
X-point to target poloidal length L_p (m)	0.05–0.15	0.05–0.25
Poloidal magnetic flux expansion f_m at OSP	16–24	3–15
Magnetic field angle at target (○)	2–5	1–2

4. Discussion

We have demonstrated experimentally that significant peak heat flux reduction simultaneously with high core plasma performance and confinement can be achieved in a high input power high current ST using the radiative divertor technique. The radiative divertor was induced by a moderate-rate, non-perturbative D_2 injection and radiation from intrinsic carbon. The significance of this result is that it was obtained in a highly shaped horizontal plate divertor configuration without active pumping, suggesting that in high-performance highly shaped ST plasmas access to reduced divertor heat flux may be naturally facilitated by SOL and divertor geometry effects. The openness of the divertor configuration is an additional benefit in this case since it enables much flexibility in the plasma shaping and performance optimization.

SOL and divertor geometry effects appear to play a prominent role in divertor transport in NSTX. Shown in table 1 are divertor parameters of the highly shaped NSTX configuration and for comparison, typical divertor parameters of a large aspect ratio tokamak, such as DIII-D [42]. Several ST geometry features that explain the observed divertor heat flux trends in NSTX are evident. First, a large in–out plasma surface area asymmetry in NSTX, along with a large Shafranov shift resulting in steep outboard gradients, lead to the heat flow distribution mostly into the outer SOL region. Second, a higher angle between B field lines and the divertor surface means that for the same $q_\parallel$, the deposited heat flux would be generally higher in an ST than in a tokamak. Third, a relatively short parallel connection length l_x between the X-point and the divertor target leads to reduced radiated power and momentum losses. The fraction of $q_\parallel$ that can be radiated is a strong function of l_x for the given impurity radiation function L_Z [43]. The momentum loss is also a function of l_x. In a shorter parallel connection length divertor, fewer ions are able to undergo collisions with neutrals and recombination events before striking the divertor surface. Finally, because of a large magnetic shear in the ST, there is a large radial gradient of the parallel connection length $\partial l_x(R)/\partial r$. The connection length is relatively short in the region adjacent to the separatrix l_x = 5–8 m (where SOL n_e is high), and becomes even shorter $l_x \sim 1$ m at a radial distance of one SOL width λ_q [13]. A steep decline in $l_x(R)$ suggests that significant power and momentum losses can be sustained only in the radial region adjacent to the separatrix, while power and particle fluxes in the far SOL may be difficult to reduce.

The divertor detachment experiments in NSTX were previously interpreted using a two-point SOL heat transport model with losses [11], a one-dimensional heat conduction SOL model with non-coronal impurity radiation (the Post model [43]), and the five region SOL model with constant power and particle sources and sinks [13, 44]. These models semi-quantitatively explained the features of the divertor regimes observed in NSTX. The models predicted that large radiated power fractions and parallel momentum loss fractions were needed to reach the OSP detachment in NSTX. Shown in figure 10 is the prediction of the Post non-coronal carbon radiation model. The model has been used to estimate divertor power losses for large aspect ratio tokamaks, e.g. ITER and DIII-D [43, 45, 46]. The model includes the heat conduction equation along the flux tube $Q_\parallel = -\kappa_0 T^{\frac{5}{2}}(\partial T_e/\partial x)$ and a power balance equation $(\partial Q_\parallel)/(\partial x) = -n_e n_Z L_Z(T_e)$, where $Q_\parallel$ is the parallel heat flux and n_Z, L_Z are the impurity density and non-coronal radiated power losses, respectively. The equations are integrated analytically to obtain the maximum power fraction that is possible to exhaust along x (or l_c) with

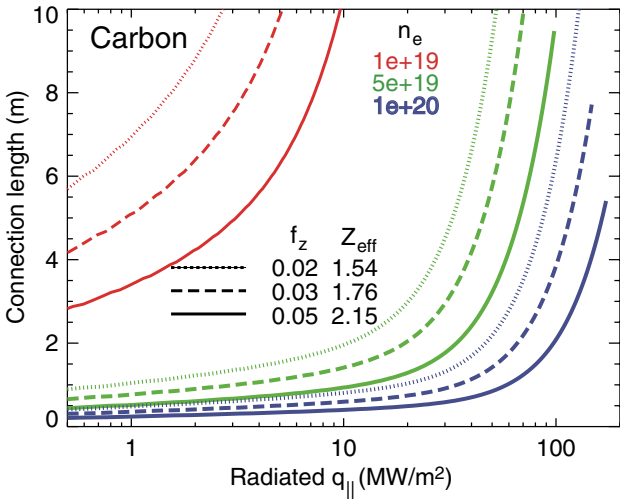

Figure 10. Predictions of parallel heat flux exhausted by non-coronal carbon radiation (the Post model) for NSTX divertor for a range of densities n_e and carbon concentrations f_z (or Z_{eff} values).

conduction losses and radiated power losses due to an impurity with a fraction f_Z. Non-coronal impurity radiation effects, namely, the charge exchange recombination effects and the impurity recycling effects, are parametrized in the model in terms of the neutral fraction n_0/n_e and the product of electron density and impurity recycling time $n_e\tau_{recy}$, respectively. For NSTX, we used $n_0/n_e = 0.1\%$, $n_e\tau_{recy} = 10^{16}\,s\,m^{-3}$, $T_e^{sep} = 60\,eV$ and $n_e^{sep} = 10^{19}\,m^3$. Since the carbon cooling curve peaks at $T_e \leqslant$ 10–60 eV for the range of non-coronal corrections applicable to NSTX, the model has little sensitivity to higher T_e^{sep} temperatures. Figure 10 demonstrates that at a typical NSTX connection length of 4–8 m, a substantial fraction of the estimated $q_{||} = 50$–$80\,MW\,m^{-2}$ can be exhausted by carbon radiation at reasonable divertor carbon and electron densities. Importantly, the required densities are consistent with NSTX divertor measurements discussed in section 3.

The simplified one-dimensional models described above did not include magnetic balance and drift effects thought to be important for divertor detachment [4]. The model also did not include two-dimensional divertor geometry effects, thought to be essential for an apparently easy access to the outer SP detachment in the highly shaped (high δ) configuration. This effect has been observed in large aspect ratio tokamaks [25, 27, 37, 47, 48], and was apparent in the NSTX divertor detachment experiments at low δ [11] and high δ [13]. The high flux expansion divertor in NSTX has a high physical divertor volume and, apparently, a higher plasma 'plugging' efficiency. The plasma 'plugging' efficiency ζ is defined as a fraction of recycling neutrals re-ionized in the divertor region. In the high flux expansion divertor ζ is higher because of the larger divertor plasma size in physical space, higher low-temperature plasma volume and thus reduced transparency to neutrals.

The geometric features of the ST SOL and divertor discussed above help explain the observed general divertor characteristics in NSTX. While highly radiative discharges with reduced divertor heat flux are not uncommon in NSTX, the PDD regime appeared to be accessible only with an additional gas injection and only in the highly shaped configuration [11, 13]. It also appears that $\bar{n}_e$ is weakly coupled with n_e^{sep} in NSTX as compared with conventional large aspect ratio tokamaks. In NSTX, the $\bar{n}_e$ increases are quite common; however, n_e^{sep} does not increase proportionally even when $\bar{n}_e$ approaches the Greenwald value [49]. This explains in part why the PDD regime does not occur spontaneously as a result of the ramping density, as the SOL collisionality in reference discharges remains at a fairly low value $\nu^*_{SOL,e} \sim$ 10–30.

Many similarities in the PDD regime properties between NSTX and conventional large aspect ratio tokamaks [25] were found. The PDD regime was characterized by a peak heat flux reduction due to radiating intrinsic carbon impurity. A reduction in divertor particle flux, apparently due to the pressure loss along the flux tube caused by ion momentum loss, and a formation of an expanding region of high-rate volume recombination, were evident. Also consistent with tokamak experiments, a long gas injection apparently resulted in an increase in the divertor density beyond a critical n_e value leading to the X-point MARFE, which in turn degraded the confinement and terminated the discharge. Further optimization of the radiative divertor regime in NSTX would be facilitated with active pumping of the divertor density.

5. Summary

Successful divertor peak heat flux mitigation in a high-power density ST with a simultaneous high core plasma confinement properties has been demonstrated in NSTX using the radiative divertor technique with D_2 injection. Divertor peak heat flux scaling developed for NSTX shows monotonic dependence on input power (and P_{SOL}) and plasma current I_p. In the highest achievable range of $P_{NBI} = 6\,MW$ and $I_p = 1.0$–$1.2\,MA$, divertor peak heat flux was reduced from 6–12 to 0.5–$2\,MW\,m^{-2}$ using high magnetic flux expansion and partial detachment of the outer strike point. This, in combination with an attractive small-ELM high-β, high bootstrap current fraction regime H-mode plasma scenario, will form a basis for high-performance scenario, development for the future ST-based concepts.

Acknowledgments

The authors thank the entire NSTX Team for technical, engineering and computer support as well as for plasma, NBI and diagnostic operations. This work was performed under the auspices of the US Department of Energy under Contracts DE-AC52-07NA27344, DE-AC02-76CH03073, DE-AC05-00OR22725 and W-7405-ENG-36.

References

[1] ITER Pphysics Expert Group on Divertor, ITER Physics Expert Group on Divertor Modelling and Database and ITER Physics Basis Editors 1999 *Nucl. Fusion* **39** 2391
[2] Lipschultz B. *et al* 2007 *Nucl. Fusion* **47** S203
[3] Ryutov D.D. *et al* 2008 *Proc. 22nd Int. Conf. on Fusion Energy 2008 (Geneva, Switzerland, 2008)* (Vienna: IAEA) CD-ROM file IC/P4-8 http://www-naweb.iaea.org/napc/physics/FEC/FEC2008/html/index.htm

[4] Petrie T.W. *et al* 2008 *Proc. 22nd Int. Conf. on Fusion Energy 2008 (Geneva, Switzerland, 2008)* (Vienna: IAEA) CD-ROM file EX/P4-21 http://www-naweb.iaea.org/napc/physics/FEC/FEC2008/html/index.htm 2009 *Nucl. Fusion* submitted

[5] Kotschenreuther M., Valanju P., Mahajan S., Zheng L.J., Pearlstein L.D., Bulmer R.H., Canik J. and Maingi R. 2008 *Proc. 22nd Int. Conf. on Fusion Energy 2008 (Geneva, Switzerland, 2008)* (Vienna: IAEA) CD-ROM file IC/P4-7 http://www-naweb.iaea.org/napc/physics/FEC/FEC2008/html/index.htm 2009 *Nucl. Fusion* submitted

[6] Lackner K. 1994 *Comment. Plasma Phys. Control. Fusion* **15** 359

[7] Maingi R. *et al* 2003 *Nucl. Fusion* **43** 969

[8] Maingi R., Kugel H.W., Lasnier C.J., Roquemore A.L., Soukhanovskii V.A. and Bush C.E. 2003 *J. Nucl. Mater.* **313–316** 1005

[9] Peng Y.-K.M. *et al* 2005 *Plasma Phys. Control. Fusion* **47** 263

[10] Goldston R.J. *et al* 2008 *Proc. 22nd Int. Conf. on Fusion Energy 2008 (Geneva, Switzerland, 2008)* (Vienna: IAEA) CD-ROM file FT/P3-12 http://www-naweb.iaea.org/napc/physics/FEC/FEC2008/html/index.htm

[11] Soukhanovskii V.A. *et al* and the NSTX Team 2006 *Proc. 21st Int. Conf. on Fusion Energy 2006 (Chengdu, China, 2006)* (Vienna: IAEA) CD-ROM file EX/P4-28 http://www-naweb.iaea.org/napc/physics/FEC/FEC2006/html/index.htm

[12] Soukhanovskii V.A. *et al* 2007 *J. Nucl. Mater.* **363–365** 432

[13] Soukhanovskii V.A. *et al* and NSTX Team 2009 *Phys. Plasmas* **16** 022501

[14] Gates D.A. *et al* 2006 *Phys. Plasmas* **13** 056122

[15] Gates D.A. *et al* 2006 *Nucl. Fusion* **46** S22

[16] Mastrovito D., Maingi R., Kugel H.W. and Roquemore A.L. 2003 *Rev. Sci. Instrum.* **74** 5090–2

[17] Soukhanovskii V.A., Roquemore A.L., Skinner C.H., Johnson D., Maingi R., Bush C., Paoletti F. and Sabbagh S. 2003 *Rev. Sci. Instrum.* **74** 2094

[18] Soukhanovskii V.A., Johnson D., Kaita R. and Roquemore A.L. 2006 *Rev. Sci. Instrum.* **77** 10F127

[19] Gunn J.P., Boucher C., Desroches D. and Robert A. 1997 *Rev. Sci. Instrum.* **68** 404

[20] Gunn J.P., Boucher C., Stansfield B.L. and Savoie S. 1995 *Rev. Sci. Instrum.* **66** 154

[21] Raman R., Kugel H.W., Gernhardt R., Provost T., Jarboe T.R. and Soukhanovskii V. 2004 *Rev. Sci. Instrum.* **75** 4347

[22] Menard J.E. *et al* 2007 *Nucl. Fusion* **47** S645

[23] Maingi R. *et al* 2005 *Nucl. Fusion* **45** 264

[24] Maingi R., Bush C.E., Kaita R., Kugel H.W., Roquemore A.L., Paul S.F. and Soukhanovskii V.A. 2007 *J. Nucl. Mater.* **363–365** 196

[25] Petrie T.W. *et al* 1997 *Nucl. Fusion* **37** 321

[26] Horton L.D. *et al* 1999 *Nucl. Fusion* **39** 1

[27] Loarte A. *et al* 1998 *Nucl. Fusion* **38** 331

[28] Soukhanovskii V.A. *et al* 2005 *J. Nucl. Mater.* **337–339** 475

[29] Whyte D.G. *et al* 2001 *Nucl. Fusion* **41** 1243

[30] Asakura N., Takenaga H., Sakurai S., Porter G.D., Rognlien T.D., Rensink M.E., Shimizu K., Higashijima S. and Kubo H. 2004 *Nucl. Fusion* **44** 503

[31] Asakura N. 2007 *J. Nucl. Mater.* **363–365** 41

[32] Paul S.F., Maingi R., Soukhanovskii V., Kaye S.M., Kugel H.W. and T.N.R. Team 2005 *J. Nucl. Mater.* **337–339** 251

[33] Fenstermacher M.E. *et al* 1999 *Plasma Phys. Control. Fusion* **41** A345

[34] Stangeby P.C. 2000 *The Plasma Boundary of Magnetic Fusion Devices* (Bristol: Institute of Physics Publishing)

[35] Fenstermacher M.E. *et al* 2003 *Plasma Phys. Control. Fusion* **45** 1597

[36] Groth M., Fenstermacher M.E., Boedo J.A., Brooks N.H., Gray D.S., Lasnier C.J., Leonard A.W., Porter G.D. and Watkins J.G. 2003 *J. Nucl. Mater.* **313–316** 1071

[37] Loarte A. 2001 *Plasma Phys. Control. Fusion* **43** 183

[38] Isler R.C., McKee G.R., Brooks N.H., West W.P., Fenstermacher M.E. and Wood R.D. 1997 *Phys. Plasmas* **4** 2989

[39] Terry J.L., Lipschultz B., Pigarov A.Yu., Krasheninnikov S.I., LaBombard B., Lumma D., Ohkawa H., Pappas D. and Umansky M. 1998 *Phys. Plasmas* **5** 1759

[40] McCracken G.M., Stamp M.F., Monk R.D., Meigs A.G., Lingertat J., Prentice R., Starling A., Smith R.J. and Tabasso A. 1998 *Nucl. Fusion* **38** 619

[41] Fenstermacher M.E. *et al* 1999 *J. Nucl. Mater.* **266** 348–53

[42] Luxon J.L. 2002 *Nucl. Fusion* **42** 614

[43] Post D., Putvinskaya N., Perkins F.W. and Nevins W. 1995 *J. Nucl. Mater.* **220–222** 1014

[44] Goswami R., Kaw P., Warrier M., Singh R. and Deshpande S. 2001 *Phys. Plasmas* **8** 857

[45] Clark R., Abdallah J. and Post D. 1995 *J. Nucl. Mater.* **220–222** 1028

[46] Post D., Abdallah J., Clark R.E.H. and Putvinskaya N. 1995 *Phys. Plasmas* **2** 2328

[47] Pitts R.A. *et al* 2001 *J. Nucl. Mater.* **290–293** 940

[48] Loarte A. 2001 *J. Nucl. Mater.* **290–293** 805–11

[49] Greenwald M. 2002 *Plasma Phys. Control. Fusion* **44** R27